

Monitoring Operational States of a Nuclear Reactor Using Seismoacoustic Signatures and Machine Learning

Chengping Chai^{*1}, Camila Ramirez², Monica Maceira¹, and Omar Marcillo¹

Abstract

Monitoring nuclear reactors is an important safety and security task with growing requirements. We explore the possibility of using seismic and acoustic data for inferring the power level of an operating reactor. Continuous data recorded at a single seismoacoustic station that is located about 50 m away from a research reactor was visualized and analyzed. The data show a clear correlation between seismoacoustic features and reactor main operational states. We designed a workflow that includes two machine learning (ML) models to classify the reactor operational states (OFF, transition, and ON) and estimate reactor power levels (10%, 30%, 50%, 70%, and 90%). We applied and compared five ML algorithms for the reactor OFF-transition-ON and four approaches for the power level classification. We also compared the performance of ML models trained with seismic-only, acoustic-only, and both types of data. Five-fold cross validations were implemented to assure a thorough evaluation of the model performances. The results show the extreme boosting gradient algorithm worked best for the first model, whereas random forests performed best for the second model. Combining seismic and acoustic data leads to better performance than using a single type of data. Seismic data contributed more than acoustic data for both models. We reached an accuracy of 0.98 for reactor OFF and ON. The accuracies for the transition state and power levels are less optimal with a minimum accuracy of 0.66. However, our results suggest seismic and acoustic data contain useful information about the transition state as well as power levels. Seismic and acoustic data could be integrated with other observations to improve monitoring performance.

Cite this article as Chai, C., C. Ramirez, M. Maceira, and O. Marcillo (2022). Monitoring Operational States of a Nuclear Reactor Using Seismoacoustic Signatures and Machine Learning, *Seismol. Res. Lett.* **XX**, 1–13, doi: [10.1785/0220210294](https://doi.org/10.1785/0220210294).

Supplemental Material

Introduction

Besides providing an accurate remote sensing method for detection of natural environmental phenomena (e.g., earthquakes, landslides, and volcanic eruptions), seismic and acoustic sensors are capable of detecting ground motions and mechanical pressure waves caused by animal movements (e.g., [Wood et al., 2005](#)), human activities (e.g., [Lecocq et al., 2020](#); [Guenaga, Marcillo, et al., 2021](#)) and industrial operations (e.g., [\(Snow, 1997; Marcillo and MacCarthy, 2020; Guenaga, Chai, et al., 2021\)](#)). For the particular case of nuclear reactors, seismic sensors have been used for building structural health evaluation (e.g., [Cho and Joe, 2005](#)), seismic hazards monitoring (e.g., [Graizer et al., 2013](#)), and seismic early warning systems (e.g., [Wieland et al., 2000](#)). Operation of machines related to nuclear reactors generate detectable seismoacoustic signals that provide us an opportunity to monitor industrial operations ([Marcillo et al., 2021](#)). However, noisy backgrounds and complex energy sources in industrial settings complicate the seismoacoustic signal and make it difficult to extract useful

information for challenging monitoring purposes such as reactor operational status and reactor power levels. Verifying that a nuclear reactor is operating as declared is of interest to the nuclear nonproliferation community. In support of exploring methods to cooperatively verify declared reactor conditions with minimally invasive techniques, we tried to develop methods to detect signals from a research nuclear reactor with seismoacoustic data.

Machine learning (ML) algorithms have shown satisfactory performance when applied to various problems in seismology (for a review see [Bergen et al., 2019](#); [Kong et al., 2019](#)), including earthquake detection and phase picking (e.g., [Yoon et al., 2015](#); [Bergen and Beroza, 2018](#); [Chen, 2018](#); [Perol et al., 2018](#);

1. Oak Ridge National Laboratory, Oak Ridge, Tennessee, U.S.A.,  <https://orcid.org/0000-0002-6792-6014> (CC);  <https://orcid.org/0000-0003-1248-2185> (MM);

2. Expedition Technology Inc., Herndon, Virginia, U.S.A.

*Corresponding author: chaic@ornl.gov

© Seismological Society of America

Ross *et al.*, 2018; Zhu and Beroza, 2018; Zhu, Peng, *et al.*, 2019; Chai *et al.*, 2020; Mousavi *et al.*, 2020), earthquake location (e.g., Zhang *et al.*, 2020), earthquake magnitude estimation (e.g., Mousavi and Beroza, 2020), earthquake focal mechanism determination (e.g., Kuang *et al.*, 2021), seismic signal discrimination (e.g., Mousavi *et al.*, 2016, 2019; Holtzman *et al.*, 2018; Li *et al.*, 2018; Martin *et al.*, 2018; Meier *et al.*, 2019; Seydoux *et al.*, 2020; Chai *et al.*, 2022), seismic signal denoising (e.g., Zhu, Mousavi, and Beroza, 2019), signal association (e.g., McBrearty *et al.*, 2019; Ross *et al.*, 2019), seismic tomography (e.g., Bianco and Gerstoft, 2018; Zhang and Lin, 2020), and laboratory earthquake prediction (e.g., Rouet-Leduc *et al.*, 2017). These ML applications not only match or surpass human performance, but also, in some cases, are able to utilize information in the raw data that is otherwise hidden. For example, statistical characteristics of continuous seismic data have been used to predict slip failure time (Rouet-Leduc *et al.*, 2017). Recent applications of transfer learning (fine-tuning pre-trained ML models) for energy-related applications (e.g., Chai *et al.*, 2020) show the great potential of ML techniques for industry settings. The number of training samples collected in industry settings is sometimes much smaller than a natural earthquake scenario. Adopting pretrained ML models through transfer learning reduces the required number of training samples significantly compared to training ML models from scratch. As physics-based models of seismic sources in industrial settings are limited and traditional analysis tools were not optimized for reactor operational monitoring, we decide to apply ML techniques to extract useful information from seismoacoustic signals for nuclear reactor operational status monitoring.

The High Flux Isotope Reactor (HFIR) at Oak Ridge National Laboratory (ORNL) is an 85 megawatt (MW) research reactor with two main states of operation, full-power operation and end-of-cycle outage. The reactor is a source of thermal and cold neutrons that are used for physics, chemistry, and biology projects. In this study, we refer to full-power operation as ON and end-of-cycle outage as OFF. The ON state lasts around 24 days, whereas the OFF state usually lasts several weeks. The intermediate state when the reactor switches from OFF to ON is called the transition state. The transition state consists of stepwise increases in power level (i.e., 10%, 30%, 50%, 70%, and 90% of 85 MW). The duration of each power level step varies from cycle to cycle. Marcillo *et al.* (2021) presented the correlation between the seismoacoustic energy and the main power of the reactor using two-month data from a seismoacoustic station located nearby HFIR. Guenaga, Chai, *et al.* (2021) detected at least 19 unique operations with a power spectral density (PSD) detector that was applied to 11-month's seismic data from the same station. Here, we focus on using ML techniques to estimate reactor operational states and power levels with one year of seismoacoustic data.

In the following section, we first describe the data we used for this study. Then, we document how we processed the data

and trained the ML models. The results on the automatic classification of reactor state (ON, OFF, or transition) and power levels for HFIR are presented afterward. ML models trained using acoustic-only, seismic-only, and both types of data were tested. We also compared the performance of five different types of ML algorithms, logistic regression (LR, Hosmer *et al.*, 2013), support vector machines (SVMs, Suykens and Vandewalle, 1999), k-nearest neighbors (KNN, Keller *et al.*, 1985), extreme gradient boosting (XGBoost, Chen and Guestrin, 2016), and random forests (RFs, Breiman, 2001). The main findings are summarized in the Summary section.

Data

Our data consist of three-channel seismograms and infrasound records collected at a single station, WACO, deployed near the HFIR buildings (Fig. 1). The station is located approximately 50 m from a cooling tower and 100 m from the HFIR main building. The WACO station includes a three-channel 4.5 Hz GeoSpace geophone and three Inter-Mountain Labs infrasound sensors. It uses a six-channel (three seismic and three acoustic channels) RefTek digitizer (RT130, Trimble) for analog to digital conversion, Global Positioning System time synchronization, and in situ storage. The RT130 digitizer is configured to have a sampling rate of 200 Hz for both seismic and acoustic channels. We used seismic and acoustic data between 23 June 2017 and 15 July 2018. We also utilized reactor power level data from the reactor monitoring system as ground truth. We refer to this data source as parametric data. Because of instrument malfunctioning and losses of power, there are some gaps (white color in Figs. 2 and 3) in the dataset. The data coverage rate (the temporal length of the recorded data over the length of the time span analyzed in this study) is 87.4% for both seismic and acoustic channels. WACO recorded seismoacoustic data associated with five occurrences of HFIR startup (two startups were missed due to data gaps). We refer to these recorded cycles as C1–C5 (as shown in Figs. 2 and 3). Though complexity undeniably exists, the operation status (ON and OFF) of HFIR correlates well with seismic and acoustic spectrograms (Figs. 2 and 3). The difference in seismic or acoustic recordings associated with different power levels does not exhibit a simple pattern (Figs. 2 and 3). We obtained the ground-truth power levels from parametric data, which were automatically measured inside the HFIR buildings. Example parametric data for cycles C2 and C3 are shown in Figure 2.

Methodology

We designed a workflow consisting of two ML models, ML models 1 and 2, to monitor operational states and power levels at HFIR using seismoacoustic data (Fig. 4). ML model 1 can be applied to continuous seismoacoustic data and estimate the state of the reactor. The data associated with the transition state can then be fed into ML model 2 to predict the reactor

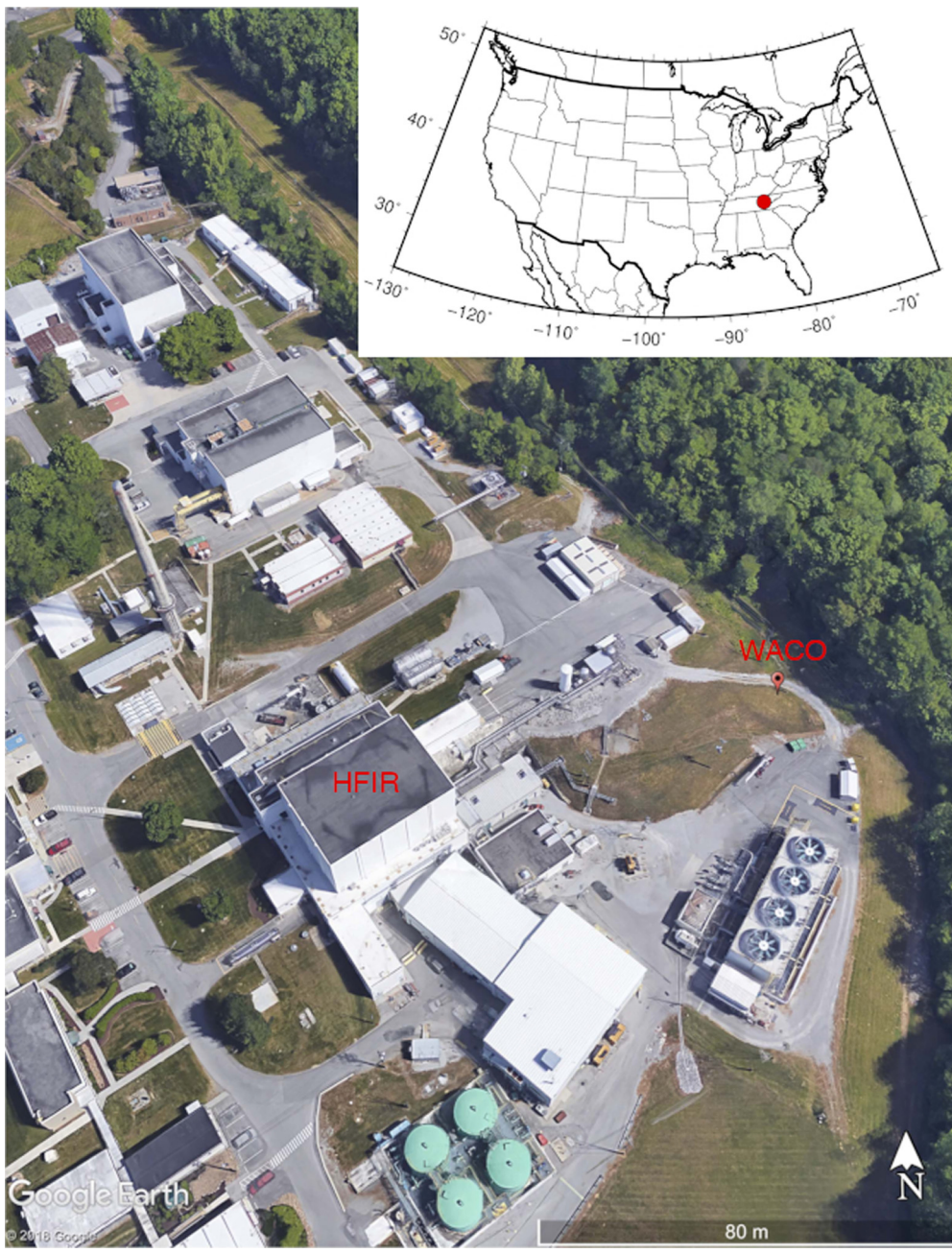
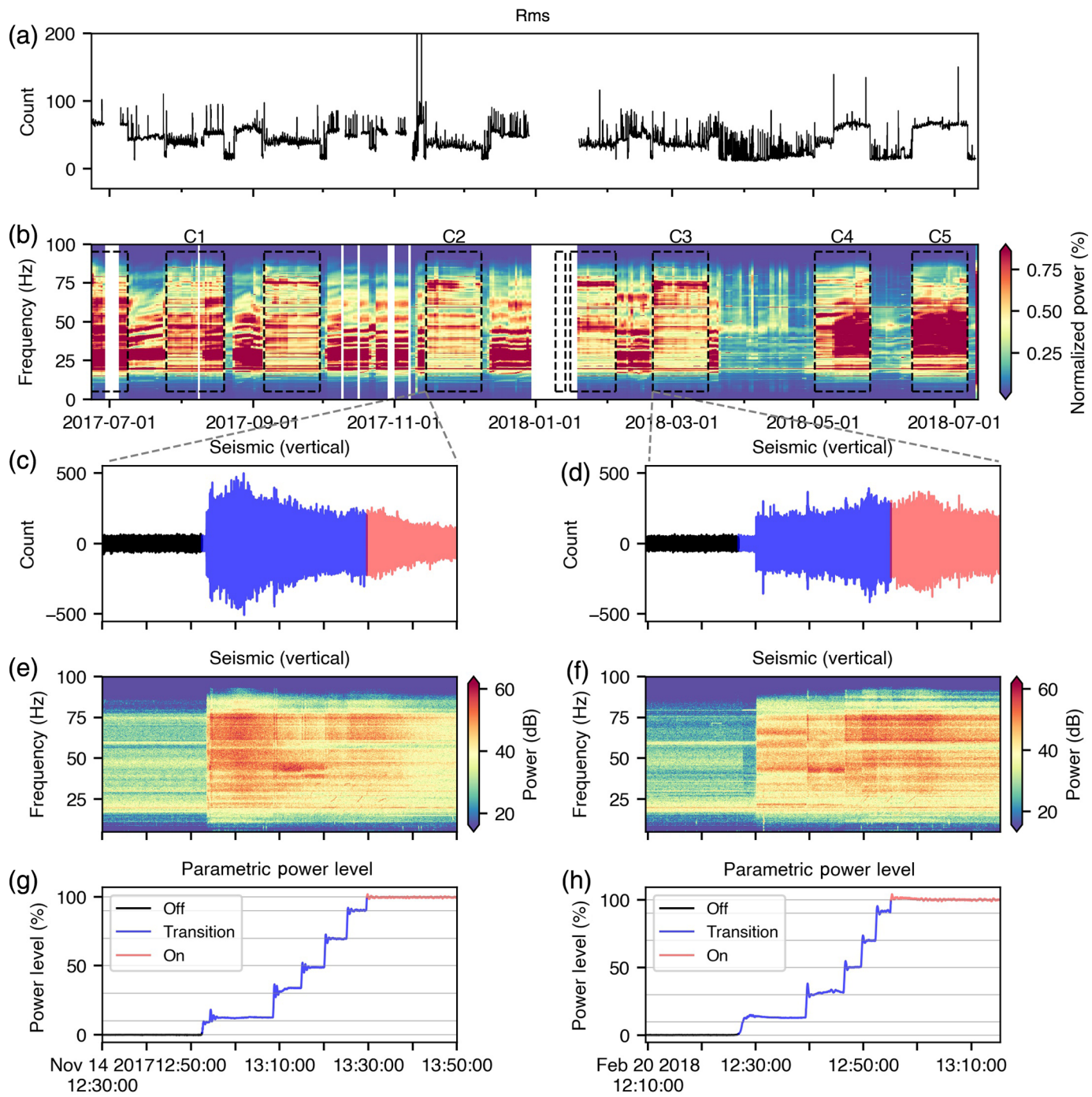


Figure 1. A satellite image from Google Earth showing the location of the seismoacoustic station WACO with respect to the High Flux Isotope Reactor (HFIR) at Oak Ridge, Tennessee. The inset shows the location of HFIR (red dot). The latitude and longitude of the bottom left corner of the satellite image is 35.9169° (north) and 84.3042° (west), respectively. The color version of this figure is available only in the electronic edition.

power levels. Because of limited data, we frame the problems into classification rather than regression. Both ML models 1 & 2 are supervised ML models that classify an input data sample into a few categories. For ML model 1, we have three categories, OFF, transition, and ON. For ML model 2, a data sample can be classified into five categories, 10%, 30%, 50%, 70%, or 90% power. These two ML models were trained independently.

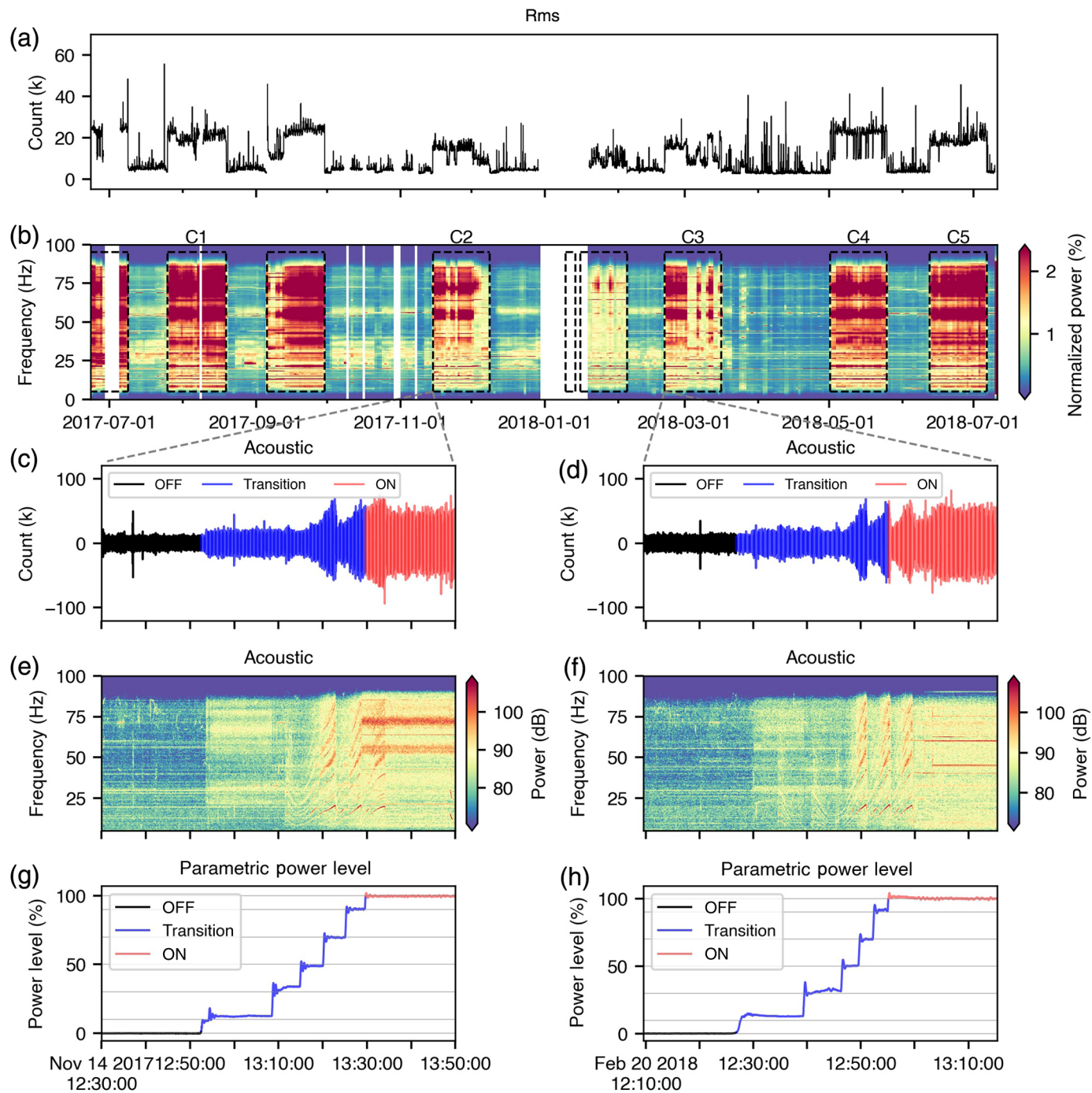
To obtain the labels (ON, OFF, or transition) for ML model 1, we first measured the timestamps of reactor state changes manually from the parametric data using interactive tools (see Chai *et al.*, 2018 for example). The resulting timestamps were then used to assign labels to data segments recorded at the seismoacoustic station for the same time span. We applied a high-pass filter with 5 Hz corner frequency to the seismic data and a 1 Hz high-pass filter to acoustic data based on the sensitivity of the sensors. The filtered data were segmented into 10-s-long time windows since shorter time windows would lead to coarser sampling in the frequencies and longer time windows would reduce the number of training samples. For each time window, we computed time-domain and frequency-domain features. Time-domain statistical features include average amplitude, absolute energy of the amplitude, kurtosis, skewness, sum of absolute first difference (see Text S1, available in the supplemental material to this article, for the equation), standard deviation, and 39 quantiles ranging from 0.025 to 0.975 with an interval of 0.025. Frequency-domain features were PSDs calculated from the 10-s-long time window without overlap. For each signal channel (vertical, north-south, east-west, or acoustic), we computed a total of 1046

features consisting of 1001 PSDs and 45 statistical features mentioned earlier. Because feature elimination (reducing the number of features with the feature importance rank) did not improve the results, we used all the features in training. The seismic data contains three channels, vertical, north-south, and east-west. We only used one channel for the acoustic data because the three acoustic channels are nearly identical



(Fig. S1). Features computed from one 10 s window are referred to as one data sample. We divided the data samples into five folds (folds 1–5) based on the time that the data were recorded (Fig. S2) so that we can evaluate ML models with cross validation. In each fold, the data were split into five subsets. Four subsets were used to train ML models (training and validation set). One subset was used for testing (test set). The subset for testing alternates among the folds so that we can more reliably evaluate the ML model performance. Each subset contains one recorded operational cycle. The labels in a subset usually start with OFF and switch to transition then move on to

Figure 2. Seismic data in (a,c,d) time domain and (b,e,f) frequency and (g,h) corresponding ground truth. (a) Root mean square (rms) of the vertical seismic component recorded at the WACO station between 23 June 2017 and 15 July 2018. (b) A year-long spectrogram of the vertical component. White space indicates data gaps. The dashed boxes represent HFIR is operating (ON). Data in the solid box are used as validation and test set for machine learning (ML) model 1. The operational cycles, C1–C5, were used for ML model 2. The color version of this figure is available only in the electronic edition.



ON and return to OFF. The training and validation set within a fold were split randomly with a ratio of 4 to 1. The validation sets were used to choose training parameters. The test sets were used to evaluate the performance of ML model 1. The datasets were standardized by subtracting the average of a corresponding training set and scaling to unit variance. We have many more data samples associated with ON and OFF than transition in the training sets (Fig. S3), which would cause ML models to favor ON and OFF over transition. To deal with this data imbalance issue, we randomly selected data samples associated with ON and OFF so that the number of data samples for each

Figure 3. Acoustic data in (a,c,d) time domain and (b,e,f) frequency and (g,h) corresponding ground truth. The boxes in (b) are the same as those in Figure 2. The color version of this figure is available only in the electronic edition.

state is the same (see Fig. S3 for an example). We used all data samples (continuous records) in the test sets to evaluate the model performance. We applied LR, SVM, KNN, XGBoost, and RF algorithms for the ML model 1. We used five nearest neighbors for the KNN. Both XGBoost and RF used 50 trees.

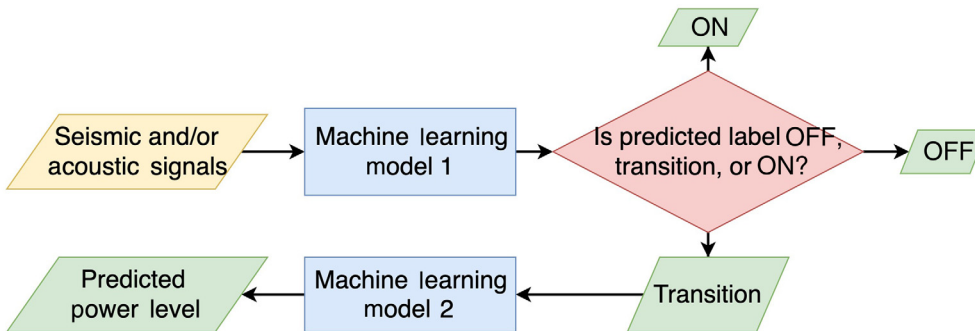


Figure 4. A flowchart shows how we use seismic and acoustic signals to predict power levels of HFIR with two ML models. The color version of this figure is available only in the electronic edition.

These parameters were selected based on the model performance for the validation sets.

We obtained power levels for the ML model 2 from parametric data. As the parametric data fluctuate around 0%, 10%, 30%, 50%, 70%, 90%, and 100%, we used a computer script to measure the timestamps of each power level. For instance, the 10% power level includes parametric data larger than 7% (3% lower than 10%) and smaller than 14% (4% higher than 10%). Data associated with fluctuations larger than (3%–4%) were excluded. The start and end times of each power level segment were stored and used to assign ground-truth power levels for acoustic and seismic data. We computed and used frequency-domain features (adding time-domain features led to lower performance) from acoustic and seismic data. The features were PSDs calculated from the 10-s-long time window with a 20% overlap. For each channel, a total of 1001 features were computed initially. We downselected the features using the feature importance (a measure of how relevant a feature is for the classification problem) from the XGBoost algorithm. Specially, we chose features that have the highest importance rates. The cumulative sum of the importance rate for the selected features is 0.999 (1 if all features are selected). The data samples were separated into the five folds in the same way as for the ML model 1. Each fold also contains five subsets. Only data samples corresponding to the transition state were used for the ML model 2. We used one subset for validation and the remaining four subsets for training. The datasets were normalized to a unit variance using a corresponding training set. Because the number of data samples for power levels differs significantly, we also randomly selected data samples for each power level so that the number of data samples is equal across different power levels (see Fig. S4 for an example). We applied LR, KNN, XGBoost, and RF algorithms for ML model 2.

Results

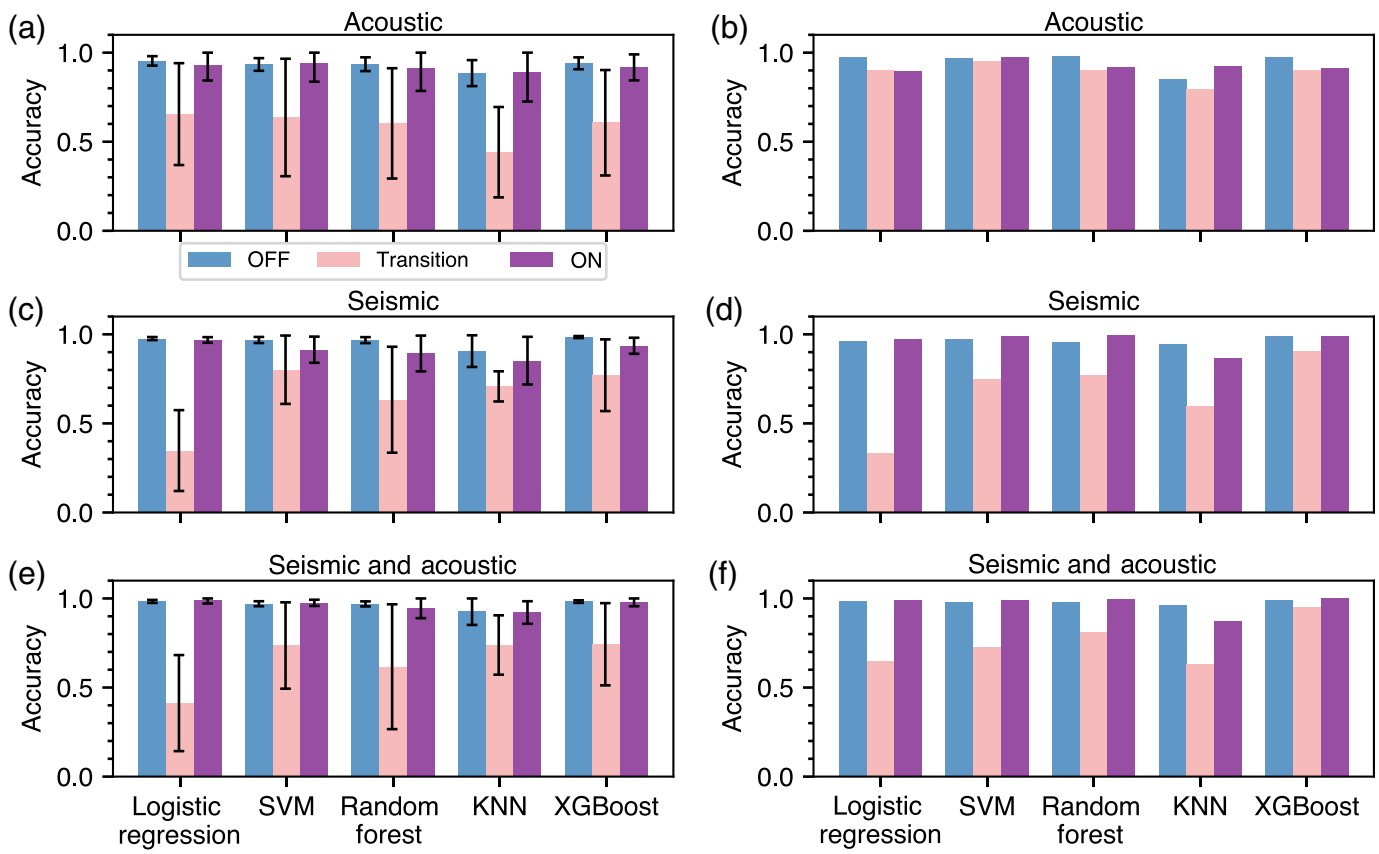
We report the performance and feature importance of ML models 1 and 2 in the following two sections.

ML model 1: OFF-transition-ON state models

As shown in Figure 5a,c,e, most ML algorithms generally work well to identify OFF and ON states. Using both seismic and acoustic data usually leads to higher accuracy (higher than 0.89) or smaller uncertainty compared to using only one type of data. The transition state is more challenging for the ML algorithms applied. We see a reduced accuracy and a large

uncertainty for the transition state. Comparing the accuracy for each fold (Figs. S5 and S6), we found the ML algorithms usually have trouble classifying the transition state for folds 4 and 5, which may be due to complex background variations in the signals. For instance, seismic and acoustic signals show significant changes after one pump near the cooling tower of HFIR failed and was replaced in early April 2018 (see Figs. 2a and 3a). RF and XGBoost have high accuracies (larger than 0.81) for transition in folds 1–3 (Figs. S5 and S6). XGBoost also has the best performance for fold two (an ideal case). XGBoost is our preferred algorithm for ML model 1. The XGBoost achieved an accuracy of 0.98 (± 0.01) for OFF, 0.74 (± 0.23) for transition, and 0.98 (± 0.02) for ON. The fold-averaged confusion matrices (a specific table summarizes the number of data samples that are correctly or incorrectly labeled for each category with respect to the ground truth) for the XGBoost algorithm are presented in Figure 6a,c,e. Though using seismic and acoustic data together decreased the accuracy (0.03) for the transition state, it led to a 0.04 improvement in accuracy for the ON state. Only 1% of the OFF labels were incorrectly classified as transition. Another 1% of the OFF labels were misclassified as ON. Only 2% of the ON labels were confused with transition. The confusion matrices for fold two (Fig. 6b,d,f) show better results when both seismic and acoustic data were used. Confusion matrices of the RF and XGBoost algorithm for each fold also show better performance in fold 1–3 when compared to fold 4–5 (Figs. S7 and S8). The (deploying) speeds of LR, RF, and XGBoost are faster than KNN and SVM (Fig. S9). The XGBoost algorithm can classify 500,000 data samples in 17.5 s (including loading the trained model and predicting labels) using 32 2.1-GHz Intel Xeon cores.

We examined the relative importance of features of the XGBoost algorithm. As shown in Figure 7, frequency-domain features account for 83.7% of the total importance rate, when the model was trained with only acoustic data. Time-domain features account for the remaining 16.3%. For the seismic-only model, frequency-domain features account for 75.5% of the total importance rate, whereas time-domain features account for 24.5%. When both seismic and acoustic data were used,



frequency-domain features account for 71.8% of the total importance rate, whereas time-domain features account for 28.2% of the total importance rate. The acoustic features account for 29.1% of the total importance rate, whereas the seismic features account for 70.9% of the total importance rate. The top six features with the highest importance rate for the XGBoost algorithm (using both seismic and acoustic data) are PSD at 10.7 Hz and absolute sum of changes of the acoustic channel, 12.5% quantile, 95% quantile, PSD at 19.8 and 43.3 Hz of the north-south seismic channel. The top 30 most influential features and their relative importance are listed in Table S1.

ML model 2: power levels models

The performance of ML algorithms shows large uncertainties (Fig. 8) for the ML model 2 that indicates significant variations in seismic and acoustic signals for different operational cycles. Using seismic data led to better performing ML models than using acoustic data. Combing seismic and acoustic data improved the performance of ML algorithms. RF outperformed LR, KNN, and XGBoost for the ML model 2. In an ideal case (fold 1), the RF algorithm achieved satisfactory accuracies for all the power levels (Fig. 8f). The best-fold-averaged accuracy is 0.77 for 10% power, 0.7 for 30%, 0.8 for 50%, 0.66 for 70%, and 0.71 for 90%. The uncertainty of these accuracies is on the order of 0.2 and 0.3. The performance varies considerably for each fold (Figs. S10–S12), which may be due to limited training data and background complexity in the data. The

Figure 5. ML model 1 performance of five different ML algorithms using (a,b) acoustic-only data, (c,d) seismic-only data, and (e,f) both seismic and acoustic data. (a,c,e) Average of five folds. (b,d,f) Results for fold 2 (an ideal case). The vertical bars in (a,c,e) indicate the standard derivation of the results from five folds. The legend is shown beneath (a). The color version of this figure is available only in the electronic edition.

components of the confusion matrix are more concentrated to the diagonal when both seismic and acoustic data were used for RF (Fig. 9). The feature importance of the random forest algorithm suggests a wide range of features contributed to the ML model 2 (Fig. 10). When both seismic and acoustic data were used, the seismic-data-derived features account for 88.4% of the total importance rate. The acoustic-data-derived features account for the remaining 11.6%. The top five features are the PSDs at 43.3, 42.7, 42.9, 42.0, and 42.4 Hz of the north-south seismic channel. The top 30 most influential features and their relative importance are listed in Table S2.

Discussion

The operations of multiple machines distributed in space at different radial distances and azimuths generate the seismic and acoustic signals that are recorded at WACO. The dominant seismic and acoustic signals are generated by machinery associated with the secondary cooling system of the reactor, mainly at the cooling tower (Marcillo *et al.*, 2021). Multiple elements such as

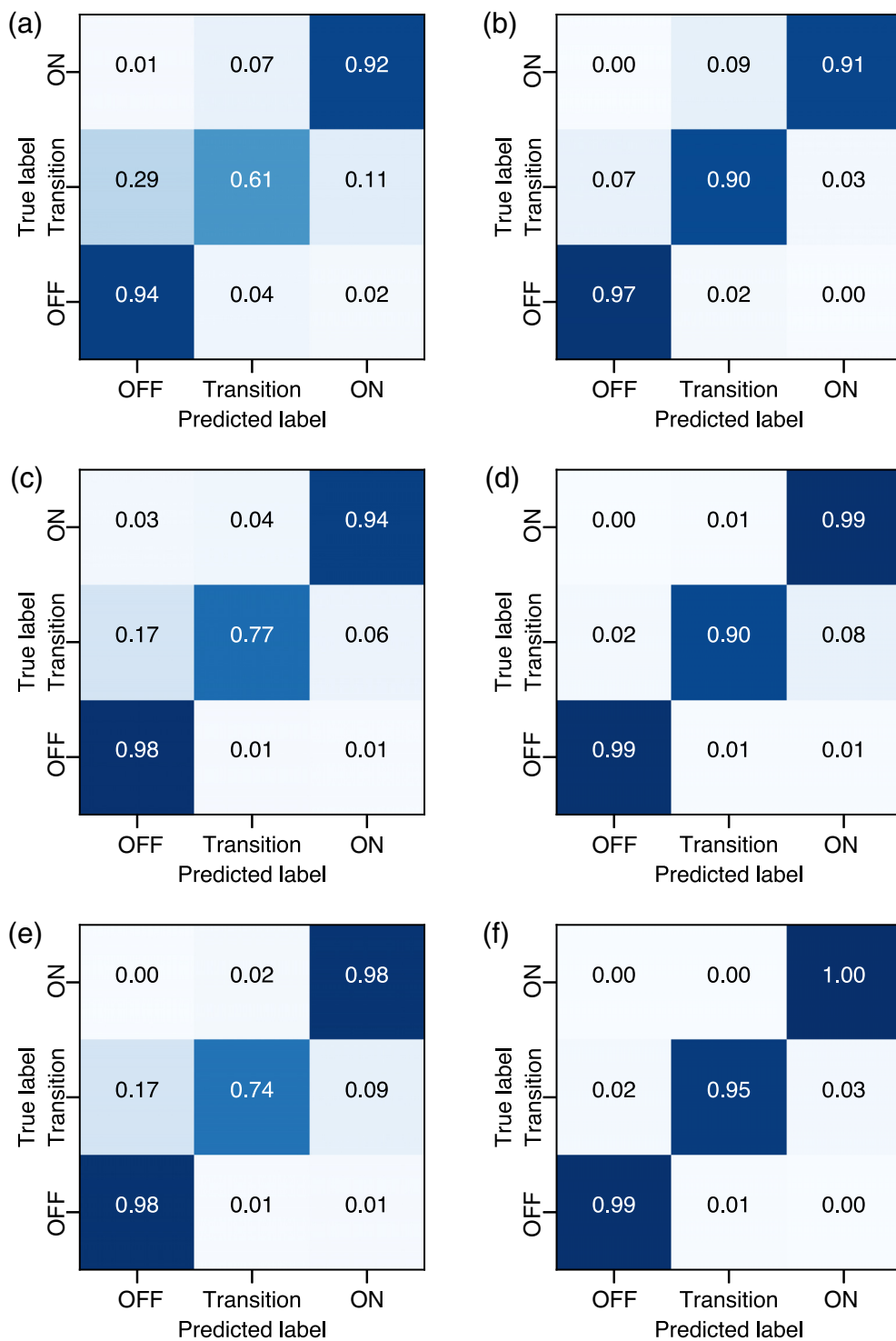


Figure 6. Confusion matrices of the XGBoost algorithm for ML model 1. (a,c,e) The average of five folds. (b,d,f) Results from fold 2 (an ideal case). Panels (a) and (b) used only acoustic data. Panels (c) and (d) used only seismic data. Panels (e) and (f) used both seismic and acoustic data. The color version of this figure is available only in the electronic edition.

pumps and fans generate mechanical energy when the reactor is operating ([Chai et al., 2021](#)). The operation of these elements changes according to the reactor operational status as well as

machinery before the reactor startup. This results in misalignment in time between patterns in the seismic and acoustic spectrograms and the power level. Another example is the

atmospheric conditions causing variations in the resulting signals. These changes can be observed during a particular cycle as well as between different cycles. Even when the reactor is in the OFF state, some instruments, such as air conditioning units and certain pumps, are still operating and together with the routine activities (e.g., test runs and maintenance) of the facility, they generate detectable seismic and acoustic signals. An interesting feature we found is the dominant seismic energy for the OFF state before April 2018, which is likely caused by the vibrations of a noisy pump. In early April 2018, this pump was replaced and the power of the seismic energy for the OFF state decreased significantly (Fig. 2a,b). We do not see this effect on the acoustic energy (Fig. 3a,b) because the pump is located on the ground and its vibrations are more effective in generating seismic waves than acoustic waves. More examples of seismically detectable operational events of HFIR can be found in [Guenaga, Chai, et al. \(2021\)](#). Because of these complexities, future studies on the physical mechanisms of the sources are needed to properly identify the location of sources and the associated machinery.

The operation of the secondary cooling system involves a large amount of machinery (e.g., pumps, fans, and valves). Not all the equipment starts to operate simultaneously with a change in reactor power level. For example, many test runs were conducted for some

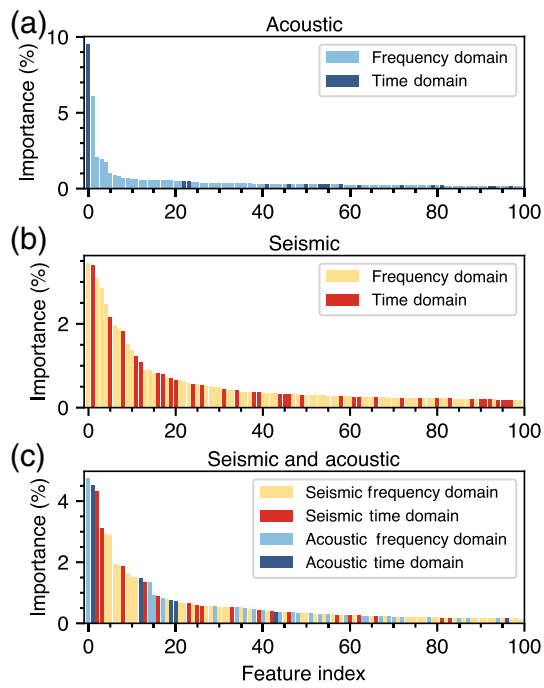


Figure 7. Relative importance of features of the XGBoost algorithm for ML model 1 using (a) acoustic-only data, (b) seismic-only data, and (c) both seismic and acoustic data. The relative importance is the average of five folds. The color version of this figure is available only in the electronic edition.

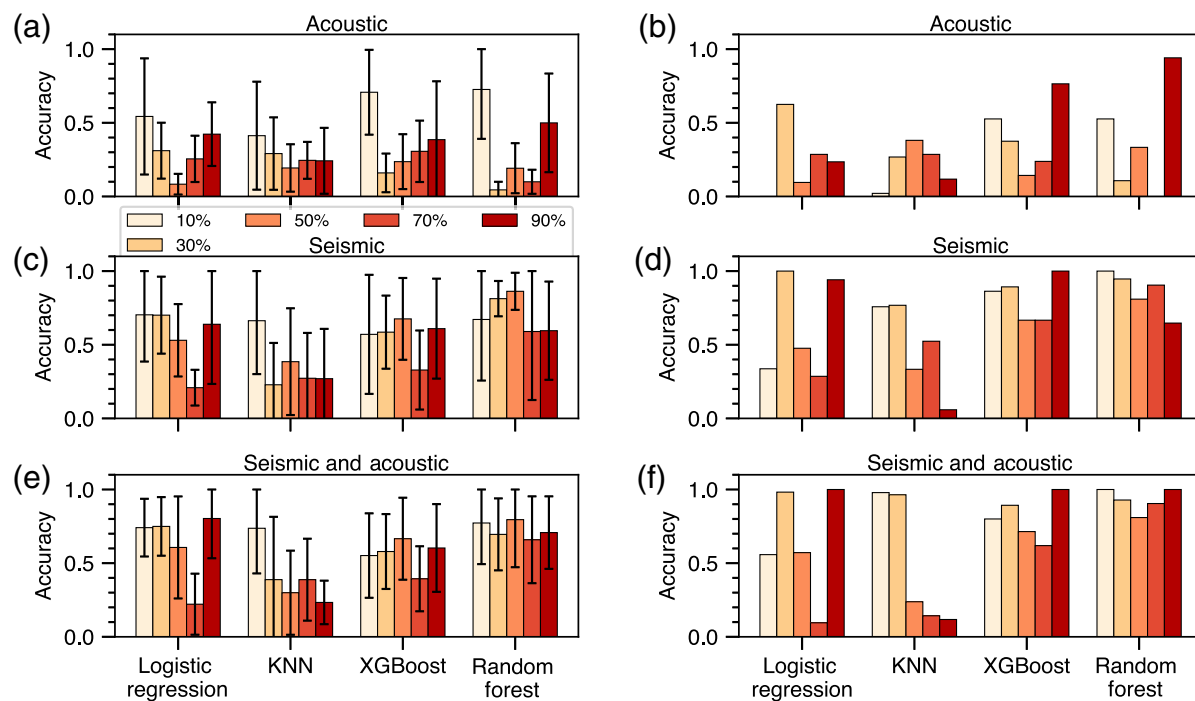


Figure 8. ML model 2 performance of four different ML algorithms using (a,b) acoustic-only data, (c,d) seismic-only data, and (e,f) both seismic and acoustic data. (a,c,e) The average of the five-fold cross validation. (b,d,f) Results from fold 1 (an ideal

patterns with increasing frequencies as a function of time during the ramp-up to full power and beginning of the ON state (see Fig. 3e,f). These patterns are associated with the two variable speed fans in the cooling tower. These two fans start operating once the reactor power level is higher than 30%–50%. These specific changes (the two examples described earlier) in the seismic and acoustic energy do not contribute to the reliable estimation of the reactor states or power levels. However, using a combination of seismic and acoustic features led to reasonable estimates of the operational states of a nuclear reactor.

The features with the highest importance rates for ML models 1 and 2 include PSDs at certain frequencies. These specific frequencies played more important roles than other features in the prediction of the operational states of the reactor or power levels. These frequencies are likely originated from the operation of certain machines that change with the reactor state. Individual features or a couple of features only account for a small portion of the total feature importance. However, combining all these features led to acceptable results. Most of the top 30 most influential features for ML models 1 and 2 are associated with data from the north-south seismic channel, which may be due to the fact the cooling tower is located to the south of the station. Using spectrograms as input features, instead of temporal and frequency features, may improve performance if sufficient training data are available. Unfortunately, we do not have enough data to train ML models

case). The vertical bars in (a,c,e) indicate the standard derivation of the results from five folds. The legend is shown beneath panel (a). The color version of this figure is available only in the electronic edition.

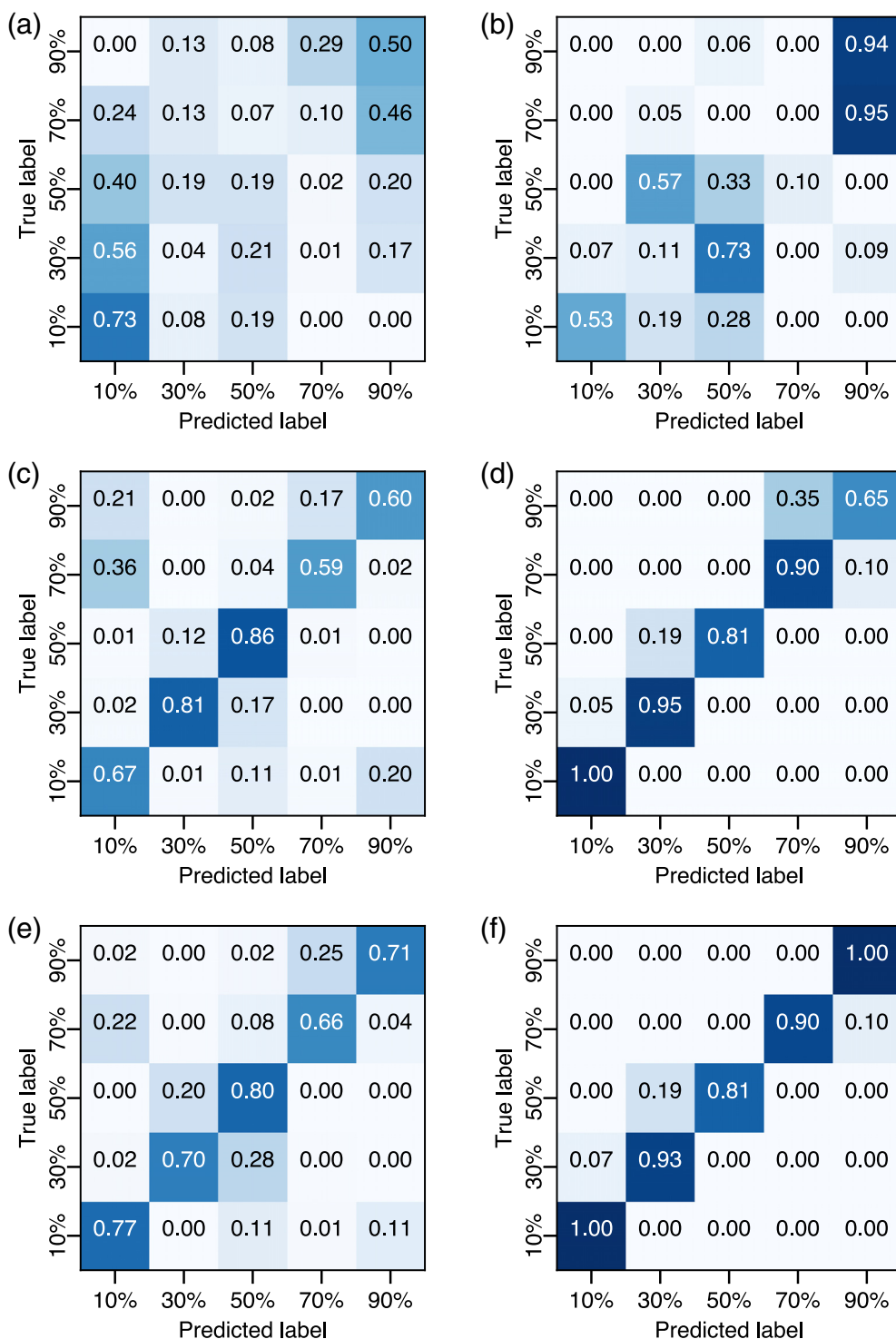


Figure 9. Confusion matrices of ML model 2 for the random forest algorithm. (a,c,e) The average of five folds. (b,d,f) Results from fold 1 (an ideal case). Panels (a) and (b) used only acoustic data. Panels (c) and (d) used only seismic data. Panels (e) and (f) used both seismic and acoustic data. The color version of this figure is available only in the electronic edition.

with spectrograms because spectrograms require longer seismograms than PSDs.

The performance of both ML models 1 and 2 is affected by factors such as the input features, the type of ML algorithm, and the parameter selections (including those related to model architecture and model training). We found the input features generally have the largest influence on the model performance. The type of ML algorithm is the second most influential factor for the model performance. The parameter selections also affect the model performance, but the influence is relatively small compared to the other factors.

Summary

We compared the performance of different ML techniques applied to continuous seismo-acoustic waveform data to characterize the operational states of the research nuclear reactor HFIR. The waveform data are retrieved from a station deployed between the main facility building and the cooling tower at HFIR. In general, our results show higher performance when classifying the ON or OFF state of the reactor than when classifying different transitional power levels. The XGBoost algorithm outperformed LR, KNN, SVM, and RF for the reactor OFF-transition-ON classification (ML model 1). Using both seismic and acoustic data and the XGBoost algorithm, we can predict the reactor OFF and ON states with an accuracy of 0.98 for continuous data. The accuracy for transition is less optimal, but the accuracy of 0.74 advocates both seismic

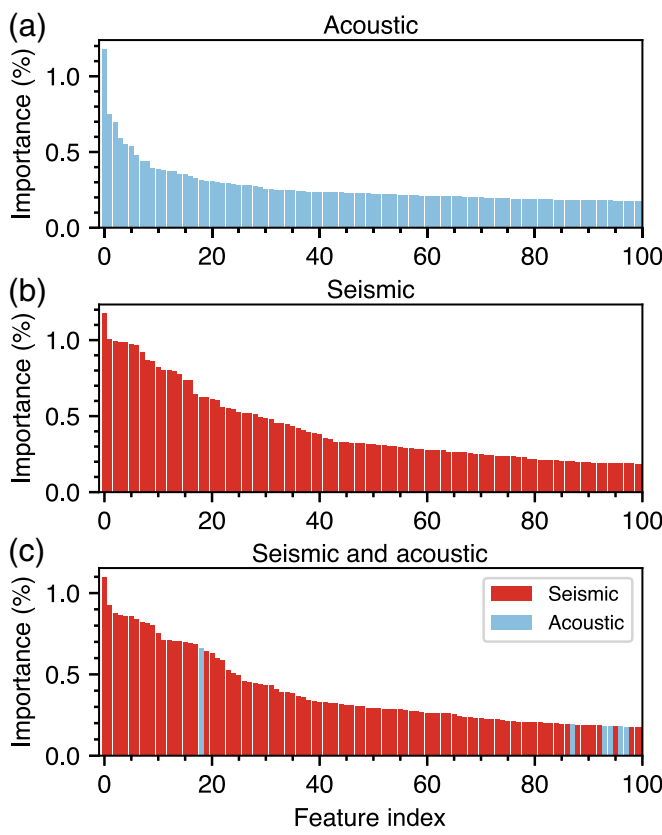


Figure 10. Relative importance of features of the random forest algorithm for ML model 2 using (a) acoustic-only data, (b) seismic-only data, and (c) both seismic and acoustic data. The color version of this figure is available only in the electronic edition.

and acoustic data carry useful information about the transition state. The RF algorithm performed better than LR, KNN, and XGboost for reactor power level classification (ML model 2). Using both seismic and acoustic data and the RF algorithm, we reached an accuracy from 0.66 to 0.8 for different power levels. Our results suggest seismic and acoustic data can provide usable information for reactor power level estimation, as the accuracy for random guessing is 0.2 (one random selection from five categories). In ideal cases (fold 2 for ML model 1 and fold 1 for ML model 2), the performance of both ML models 1 and 2 is clearly satisfactory (accuracies for all categories are larger than 0.9 except for the 50% power level). When used individually, seismic data performed better than acoustic data for both ML models 1 and 2. We also found that integrating seismic and acoustic data led to better results than using just one type of data for both ML models 1 and 2. A wide range of features computed from seismic and acoustic data contributed to the ML models, including PSD at 10.7 Hz on the acoustic channel, and PSDs at 19.8, 42, 42.4, 42.7, 42.9, and 43.3 Hz on the north-south seismic channel. Frequency-domain features contributed more than time-domain counterparts for the ML model 1, which may be due to better correlations

(Figs. 2 and 3) between the frequency-domain features and reactor operational states. Seismic features played a larger role than acoustic features for both ML models 1 and 2. Incorporating other types of observations such as thermal signals and more sophisticated ML models may improve the performance.

Data and Resources

Waveform and parametric data used in this study are available by request only. An External Computer Access Management System (XCAMS) account and formal request must be made to gain access to waveform data through Oak Ridge National Laboratory's (ORNL's) XCAMS website (<https://xcams.ornl.gov/xcams/>). For assistance on obtaining an XCAMS account, please contact the ORNL Computer Helpline at 865-241-6765 or send an e-mail requesting assistance to helpline@ornl.gov. For further assistance accessing data, please contact Monica Maceira (maceiram@ornl.gov). Most figures were prepared with Generic Mapping Tools version 5.4.4 (GMT, v.5.4.4., Wessel *et al.*, 2013) and Matplotlib v.3.3.3 (Hunter, 2007). NumPy v.1.20.1 (Van Der Walt *et al.*, 2011) and ObsPy v.1.2.2 (Beyreuther *et al.*, 2010; Megies *et al.*, 2011; Krischer *et al.*, 2015) were used to process the seismic data. Scikit-learn v.0.23.2 (Pedregosa *et al.*, 2011) was used to train machine learning (ML) models. Figure 1 used satellite images from Google Earth (<https://www.google.com/earth/>). All websites were last accessed in July 2021. The supplemental material for this article includes details on the calculation of the sum of absolute first difference (Text S1); a figure showing a comparison of the three acoustic channels (Fig. S1); a figure showing the partition of the five folds used for cross validation (Fig. S2); a comparison of number of data samples before and after random sampling for the ML model 1 (Fig. S3); a comparison of number of data samples before and after random sampling for the ML model 2 (Fig. S4); a comparison of ML model 1 accuracy of the random forest algorithm for each fold (Fig. S5); a comparison of ML model 1 accuracy of the extreme gradient boosting algorithm (Fig. S6); a comparison of ML model 1 confusion matrices for the random forest algorithm (Fig. S7); a comparison of ML model 1 confusion matrices for the extreme gradient boosting algorithm (Fig. S8); a comparison of runtime as a function of number of data samples for different ML model 1 algorithms (Fig. S9); a comparison of ML model 2 accuracy of the random forest algorithm for each fold (Fig. S10); a comparison of ML model 2 confusion matrices for the random forest algorithm (Fig. S11); a comparison of ground-truth power levels and predicted power levels using the random forest algorithm (Fig. S12); a table listing the top 30 features of the XGBoost algorithm for ML model 1 (Table S1); and a table listing the top 30 features of the random forest algorithm for ML model 2 (Table S2).

Declaration of Competing Interests

The authors acknowledge that there are no conflicts of interest recorded.

Acknowledgments

The work described in this article was funded by the U.S. National Nuclear Security Administration, Defense Nuclear Nonproliferation Research and Development, Office of Proliferation Detection. This

article has been authored in part by UT-Battelle, LLC, under Contract Number DE-AC05-00OR22725 with the US Department of Energy (DOE). This research used resources at the High Flux Isotope Reactor (HFIR), a DOE Office of Science User Facility operated by the Oak Ridge National Laboratory (ORNL). This research used resources of the Compute and Data Environment for Science (CADES) at the ORNL, which is supported by the Office of Science of the U.S. Department of Energy under Contract Number DE-AC05-00OR22725. The U.S. Government retains and the publisher, by accepting the article for publication, acknowledges that the U.S. Government retains a nonexclusive, paid-up, irrevocable, worldwide license to publish or reproduce the published form of this article, or allow others to do so, for U.S. Government purposes. DOE will provide public access to these results of federally sponsored research in accordance with the DOE Public Access Plan (<http://energy.gov/downloads/doe-public-access-plan>, last accessed January 2022). The views and conclusions contained in this document are those of the authors and should not be interpreted as necessarily representing the official policies, either expressed or implied, of the U.S. Government. The authors acknowledge that there are no conflicts of interest recorded. The authors thank Jason Hite for helpful suggestions. The authors thank the Editor Allison Bent, and two anonymous reviewers for their constructive comments.

References

- Bergen, K. J., and G. C. Beroza (2018). Detecting earthquakes over a seismic network using single-station similarity measures, *Geophys. J. Int.* **213**, no. 3, 1984–1998, doi: [10.1093/gji/ggy100](https://doi.org/10.1093/gji/ggy100).
- Bergen, K. J., P. A. Johnson, M. V. de Hoop, and G. C. Beroza (2019). Machine learning for data-driven discovery in solid Earth geoscience, *Science* **363**, no. 6433, eaau0323, doi: [10.1126/science.aau0323](https://doi.org/10.1126/science.aau0323).
- Beyreuther, M., R. Barsch, L. Krischer, T. Megies, Y. Behr, and J. Wassermann (2010). ObsPy: A python toolbox for seismology, *Seismol. Res. Lett.* **81**, no. 3, 530–533, doi: [10.1785/gssrl.81.3.530](https://doi.org/10.1785/gssrl.81.3.530).
- Bianco, M. J., and P. Gerstoft (2018). Travel time tomography with adaptive dictionaries, *IEEE Trans. Comput. Imaging* **4**, no. 4, 499–511, doi: [10.1109/TCI.2018.2862644](https://doi.org/10.1109/TCI.2018.2862644).
- Breiman, L. (2001). Random forest, *Machine Learn.* **45**, 5–32, doi: [10.1023/A:1010933404324](https://doi.org/10.1023/A:1010933404324).
- Chai, C., C. J. Ammon, M. Maceira, and R. B. Herrmann (2018). Interactive visualization of complex seismic data and models using Bokeh, *Seismol. Res. Lett.* **89**, no. 2A, 668–676, doi: [10.1785/0220170132](https://doi.org/10.1785/0220170132).
- Chai, C., J. Kintner, K. M. Cleveland, J. Luo, M. Maceira, and C. J. Ammon (2022). Automatic waveform quality control for surface waves using machine learning, *Seismol. Res. Lett.* doi: [10.1785/0220210302](https://doi.org/10.1785/0220210302).
- Chai, C., M. Maceira, and O. Marcillo (2021). *Seismo-Acoustic Characteristics of HFIR Cooling Tower Fans and Pumps*, Oak Ridge, Tennessee, available at <https://www.osti.gov/biblio/1838965> (last accessed January 2022).
- Chai, C., M. Maceira, H. J. Santos-Villalobos, S. V. Venkatakrishnan, M. Schoenball, W. Zhu, G. C. Beroza, C. Thurber, and EGS Collab Team (2020). Using a deep neural network and transfer learning to bridge scales for seismic phase picking, *Geophys. Res. Lett.* **47**, no. 16, e2020GL088651, doi: [10.1029/2020GL088651](https://doi.org/10.1029/2020GL088651).
- Chen, Y. (2018). Automatic microseismic event picking via unsupervised machine learning, *Geophys. J. Int.* **212**, no. 1, 88–102, doi: [10.1093/gji/ggx420](https://doi.org/10.1093/gji/ggx420).
- Chen, T., and C. Guestrin (2016). XGBoost: A scalable tree boosting system, *Proc. of the 22nd ACM SIGKDD International Conf. Knowledge Discovery and Data Mining*, ACM, 785–794, doi: [10.1145/2939672.2939785](https://doi.org/10.1145/2939672.2939785).
- Cho, S. G., and Y. H. Joe (2005). Seismic fragility analyses of nuclear power plant structures based on the recorded earthquake data in Korea, *Nucl. Eng. Des.* **235**, nos. 17/19, 1867–1874, doi: [10.1016/j.nucengdes.2005.05.021](https://doi.org/10.1016/j.nucengdes.2005.05.021).
- Graizer, V., C. G. Munson, and Y. Li (2013). North Anna nuclear power plant strong-motion records of the mineral, Virginia, earthquake of 23 August 2011, *Seismol. Res. Lett.* **84**, no. 3, 551–557, doi: [10.1785/0220120138](https://doi.org/10.1785/0220120138).
- Guenaga, D. L., C. Chai, M. Maceira, O. E. Marcillo, and A. A. Velasco (2021). Seismically detecting nuclear reactor operations using a power spectral density (PSD) misfit detector, *Bull. Seismol. Soc. Am.* **111**, no. 3, 1378–1391, doi: [10.1785/0120200267](https://doi.org/10.1785/0120200267).
- Guenaga, D. L., O. E. Marcillo, A. A. Velasco, C. Chai, and M. Maceira (2021). The silencing of U.S. campuses following the COVID-19 response: Evaluating root mean square seismic amplitudes using power spectral density data, *Seismol. Res. Lett.* **92**, no. 2A, 941–950, doi: [10.1785/0220200391](https://doi.org/10.1785/0220200391).
- Holtzman, B. K., A. Paté, J. Paisley, F. Waldhauser, and D. Repetto (2018). Machine learning reveals cyclic changes in seismic source spectra in Geysers geothermal field, *Sci. Adv.* **4**, no. 5, 1–8, doi: [10.1126/sciadv.aoa2929](https://doi.org/10.1126/sciadv.aoa2929).
- Hosmer, D. W., Jr, S. Lemeshow, and R. X. Sturdivant (2013). *Applied Logistic Regression*, John Wiley and Sons, Inc., Hoboken, New Jersey.
- Hunter, J. D. (2007). Matplotlib: A 2D graphics environment, *Comput. Sci. Eng.* **9**, no. 3, 90–95, doi: [10.1109/MCSE.2007.55](https://doi.org/10.1109/MCSE.2007.55).
- Keller, J. M., M. R. Gray, and J. A. Givens (1985). A fuzzy K-nearest neighbor algorithm, *IEEE Trans. Syst. Man. Cybern. SMC-15*, no. 4, 580–585, doi: [10.1109/TSMC.1985.6313426](https://doi.org/10.1109/TSMC.1985.6313426).
- Kong, Q., D. T. Trugman, Z. E. Ross, M. J. Bianco, B. J. Meade, and P. Gerstoft (2019). Machine learning in seismology: Turning data into insights, *Seismol. Res. Lett.* **90**, no. 1, 3–14, doi: [10.1785/0220180259](https://doi.org/10.1785/0220180259).
- Krischer, L., T. Megies, R. Barsch, M. Beyreuther, T. Lecocq, C. Caudron, and J. Wassermann (2015). ObsPy: A bridge for seismology into the scientific Python ecosystem, *Comput. Sci. Discov.* **8**, no. 1, 014003, doi: [10.1088/1749-4699/8/1/014003](https://doi.org/10.1088/1749-4699/8/1/014003).
- Kuang, W., C. Yuan, and J. Zhang (2021). Real-time determination of earthquake focal mechanism via deep learning, *Nat. Commun.* **12**, no. 1, 1432, doi: [10.1038/s41467-021-21670-x](https://doi.org/10.1038/s41467-021-21670-x).
- Lecocq, T., S. P. Hicks, K. Van Noten, K. van Wijk, P. Koelmeijer, R. S. M. De Plaen, F. Massin, G. Hillers, R. E. Anthony, M. Apoloner, et al. (2020). Global quieting of high-frequency seismic noise due to COVID-19 pandemic lockdown measures, *Science* **369**, no. 6509, 1338–1343, doi: [10.1126/science.abd2438](https://doi.org/10.1126/science.abd2438).
- Li, Z., M. A. Meier, E. Hauksson, Z. Zhan, and J. Andrews (2018). Machine learning seismic wave discrimination: Application to earthquake early warning, *Geophys. Res. Lett.* **45**, no. 10, 4773–4779, doi: [10.1029/2018GL077870](https://doi.org/10.1029/2018GL077870).

- Marcillo, O. E., and J. MacCarthy (2020). Mapping seismic tonal noise in the contiguous United States, *Seismol. Res. Lett.* **91**, no. 3, 1707–1716, doi: [10.1785/0220190355](https://doi.org/10.1785/0220190355).
- Marcillo, O. E., M. Maceira, C. Chai, C. Gammans, R. Hunley, and C. Young (2021). The local seismoacoustic wavefield of a research nuclear reactor and its response to reactor power level, *Seismol. Res. Lett.* **92**, no. 1, 378–387, doi: [10.1785/0220200139](https://doi.org/10.1785/0220200139).
- Martin, E. R., F. Huot, Y. Ma, R. Cieplicki, S. Cole, M. Karrenbach, and B. L. Biondi (2018). A seismic shift in scalable acquisition demands new processing: Fiber-optic seismic signal retrieval in Urban Areas with unsupervised learning for coherent noise removal, *IEEE Signal Process. Mag.* **35**, no. 2, 31–40, doi: [10.1109/MSP.2017.2783381](https://doi.org/10.1109/MSP.2017.2783381).
- McBrearty, I. W., A. A. Delorey, and P. A. Johnson (2019). Pairwise association of seismic arrivals with convolutional neural networks, *Seismol. Res. Lett.* **90**, no. 2A, 503–509, doi: [10.1785/0220180326](https://doi.org/10.1785/0220180326).
- Megies, T., M. Beyreuther, R. Barsch, L. Krischer, and J. Wassermann (2011). ObsPy—What can it do for data centers and observatories? *Ann. Geophys.* **54**, no. 1, 47–58, doi: [10.4401/ag-4838](https://doi.org/10.4401/ag-4838).
- Meier, M. A., Z. E. Ross, A. Ramachandran, A. Balakrishna, S. Nair, P. Kundzicz, Z. Li, J. Andrews, E. Hauksson, and Y. Yue (2019). Reliable real-time seismic signal/noise discrimination with machine learning, *J. Geophys. Res.* **124**, no. 1, 788–800, doi: [10.1029/2018JB016661](https://doi.org/10.1029/2018JB016661).
- Mousavi, S. M., and G. C. Beroza (2020). A machine-learning approach for earthquake magnitude estimation, *Geophys. Res. Lett.* **47**, no. 1, 1–7, doi: [10.1029/2019GL085976](https://doi.org/10.1029/2019GL085976).
- Mousavi, S. M., W. L. Ellsworth, W. Zhu, L. Y. Chuang, and G. C. Beroza (2020). Earthquake transformer—An attentive deep-learning model for simultaneous earthquake detection and phase picking, *Nat. Commun.* **11**, no. 1, 3952, doi: [10.1038/s41467-020-17591-w](https://doi.org/10.1038/s41467-020-17591-w).
- Mousavi, S. M., S. P. Horton, C. A. Langston, and B. Samei (2016). Seismic features and automatic discrimination of deep and shallow induced-microearthquakes using neural network and logistic regression, *Geophys. J. Int.* **207**, no. 1, 29–46, doi: [10.1093/gji/ggw258](https://doi.org/10.1093/gji/ggw258).
- Mousavi, S. M., W. Zhu, W. Ellsworth, and G. Beroza (2019). Unsupervised clustering of seismic signals using deep convolutional autoencoders, *IEEE Geosci. Remote Sens. Lett.* **16**, no. 11, 1693–1697, doi: [10.1109/LGRS.2019.2909218](https://doi.org/10.1109/LGRS.2019.2909218).
- Pedregosa, F., G. Varoquaux, A. Gramfort, V. Michel, B. Thirion, O. Grisel, M. Blondel, P. Prettenhofer, R. Weiss, V. Dubourg, et al. (2011). Scikit-learn: Machine learning in Python, *J. Mach. Learn. Res.* **12**, 2825–2830.
- Perol, T., M. Gharbi, and M. Denolle (2018). Convolutional neural network for earthquake detection and location, *Sci. Adv.* **4**, no. 2, e1700578 , doi: [10.1126/sciadv.1700578](https://doi.org/10.1126/sciadv.1700578).
- Ross, Z. E., M.-A. Meier, and E. Hauksson (2018). P wave arrival picking and first-motion polarity determination with deep learning, *J. Geophys. Res.* **123**, no. 6, 5120–5129, doi: [10.1029/2017JB015251](https://doi.org/10.1029/2017JB015251).
- Ross, Z. E., Y. Yue, M. Meier, E. Hauksson, and T. H. Heaton (2019). PhaseLink: A deep learning approach to seismic phase association, *J. Geophys. Res.* **124**, no. 1, 856–869, doi: [10.1029/2018JB016674](https://doi.org/10.1029/2018JB016674).
- Rouet-Leduc, B., C. Hulbert, N. Lubbers, K. Barros, C. J. Humphreys, and P. A. Johnson (2017). Machine learning predicts laboratory earthquakes, *Geophys. Res. Lett.* **44**, no. 18, 9276–9282, doi: [10.1002/2017GL074677](https://doi.org/10.1002/2017GL074677).
- Seydoux, L., R. Balestrieri, P. Poli, M. de Hoop, M. Campillo, and R. Baraniuk (2020). Clustering earthquake signals and background noises in continuous seismic data with unsupervised deep learning, *Nat. Commun.* **11**, no. 1, doi: [10.1038/s41467-020-17841-x](https://doi.org/10.1038/s41467-020-17841-x).
- Snow, D. J. (1997). Noise control in power plant, *Proc. Inst. Mech. Eng. Part A J. Power Energy* **211**, no. 1, 73–93, doi: [10.1243/0957650971537015](https://doi.org/10.1243/0957650971537015).
- Suykens, J. A. K., and J. Vandewalle (1999). Least squares support vector machine classifiers, *Neural Process. Lett.* **9**, 293–300, doi: [10.1023/A:1018628609742](https://doi.org/10.1023/A:1018628609742).
- Van Der Walt, S., S. C. Colbert, and G. Varoquaux (2011). The NumPy array: A structure for efficient numerical computation, *Comput. Sci. Eng.* **13**, no. 2, 22–30, doi: [10.1109/MCSE.2011.37](https://doi.org/10.1109/MCSE.2011.37).
- Wessel, P., W. H. F. Smith, R. Scharroo, J. Luis, and F. Wobbe (2013). Generic Mapping Tools: Improved version released, *Eos Trans. AGU* **94**, no. 45, 409–410, doi: [10.1002/2013EO450001](https://doi.org/10.1002/2013EO450001).
- Wieland, M., L. Griesser, and C. Kuendig (2000). Seismic early warning system for a nuclear power plant, *Proc. 12th World Conf. Earthquake Engineering (WCEE 2000)*, Auckland, New Zealand, 30 January–4 February 2000.
- Wood, J. D., C. E. O'Connell-Rodwell, and S. L. Klemperer (2005). Using seismic sensors to detect elephants and other large mammals: A potential census technique, *J. Appl. Ecol.* **42**, no. 3, 587–594, doi: [10.1111/j.1365-2664.2005.01044.x](https://doi.org/10.1111/j.1365-2664.2005.01044.x).
- Yoon, C. E., O. O'Reilly, K. J. Bergen, and G. C. Beroza (2015). Earthquake detection through computationally efficient similarity search, *Sci. Adv.* **1**, no. 11, e1501057 , doi: [10.1126/sciadv.1501057](https://doi.org/10.1126/sciadv.1501057).
- Zhang, Z., and Y. Lin (2020). Data-driven seismic waveform inversion: A study on the robustness and generalization, *IEEE Trans. Geosci. Remote Sens.* **58**, no. 10, 6900–6913, doi: [10.1109/TGRS.2020.2977635](https://doi.org/10.1109/TGRS.2020.2977635).
- Zhang, X., J. Zhang, C. Yuan, S. Liu, Z. Chen, and W. Li (2020). Locating induced earthquakes with a network of seismic stations in Oklahoma via a deep learning method, *Sci. Rep.* **10**, no. 1, doi: [10.1038/s41598-020-58908-5](https://doi.org/10.1038/s41598-020-58908-5).
- Zhu, W., and G. C. Beroza (2018). PhaseNet: A deep-neural-network-based seismic arrival time picking method, *Geophys. J. Int.* **216**, no. 1, 261–273, doi: [10.1093/gji/ggy423](https://doi.org/10.1093/gji/ggy423).
- Zhu, L., Z. Peng, J. McClellan, C. Li, D. Yao, Z. Li, and L. Fang (2019). Deep learning for seismic phase detection and picking in the aftershock zone of 2008 M7.9 Wenchuan Earthquake, *Phys. Earth Planet. In.* **293**, 106261, doi: [10.1016/j.pepi.2019.05.004](https://doi.org/10.1016/j.pepi.2019.05.004).
- Zhu, W., S. M. Mousavi, and G. C. Beroza (2019). Seismic signal denoising and decomposition using deep neural networks, *IEEE Trans. Geosci. Remote Sens.* **57**, no. 11, 9476–9488, doi: [10.1109/TGRS.2019.2926772](https://doi.org/10.1109/TGRS.2019.2926772).

Manuscript received 18 October 2021

Published online 9 March 2022